EPJ *Photovoltaics*

REGULAR ARTICLE

OPEN ACCESS

Improvement of hetero-interface engineering by partial substitution of Zn in Cu_2ZnSnS_4-based solar cells

Charif Tamin[1,2,3,*] , Denis Chaumont[1], Olivier Heintz[1], Aymeric Leray[1], and Mohamed Adnane[2]

[1] Laboratoire Interdisciplinaire Carnot de Bourgogne (ICB UMR 6303 CNRS), Université de Bourgogne Franche-Comté, BP 47 870, 21078 Dijon, France

[2] Laboratoire de Microscopie Electronique et Sciences des Matériaux (LMESM), Université des Sciences et de la Technologie d'Oran Mohamed Boudiaf USTO-MB, El M'naouar BP 1505, Bir El Djir, 31000 Oran, Algeria

[3] Univ. Lyon, INSA Lyon, CNRS, Ecole Centrale de Lyon, Université Claude Bernard Lyon 1, CPE Lyon, INL, UMR 5270, 69621 Villeurbanne, France

Abstract. This paper investigates the effects of partial substitution of zinc (Zn) in pure sulfide kesterite (Cu_2ZnSnS_4) by cadmium (Cd) and manganese (Mn) incorporation. Thin films of Cu_2ZnSnS_4 (CZTS), $Cu_2Zn_{1-x}Cd_xSnS_4$ (CCZTS) and $Cu_2Zn_{1-x}Mn_xSnS_4$(CMZTS) were produced chemically. A comparison of pure CZTS with CCZTS and CMZTS was performed to study the influence of Cd and Mn incorporation on the morphology, structure, optical and electronic properties of the films. The results show an improvement of the morphology and an adjustment of the band gap and valence band position by partial substitution of Zn with Cd and Mn. In addition, for the first time, the band alignment at the absorber/buffer hetero-interface is studied with partial Zn substitution. Band alignments at the absorber/buffer hetero-interface were estimated by XPS and UV/Visible measurements. The results show a cliff-like CBO for CZTS/CdS heterojunction, a spike-like CBO for CCZTS/CdS and a near flat-band CBO for CMZTS/CdS heterojunction.

Keywords: Kesterite / solar cell / cation substitution / band alignment

1 Introduction

The photovoltaic (PV) cell market is dominated by 90% crystalline silicon, but the PV conversion efficiency of this technology is close to its Shockley-Queisser (SQ) limit (29.1%) [1]. However, silicon-based solar cells require several tens of microns ($\sim$180 µm) of high-quality crystalline silicon to generate a high photovoltaic conversion efficiency. Thus, the generation of thin-film solar cells has emerged in order to reduce the thickness of solar cells, the production cost and to develop thin-film solar cells suitable for various applications such as building and product integrated photovoltaics (BIPV and PIPV). Three technologies are currently under development on an industrial scale: amorphous silicon (a-Si), cadmium telluride (CdTe) and $CuIn_{1-x}Ga_x(S,S_e)_2$ alloys (CIGSSe). CIGSSe-based alloy technologies have reached efficiency levels of 23.35%, which is higher than CdTe and a-Si [2,3]. However, the efficiency of pure sulfide CIGS is 16% as presented recently by Barreau et al. for a bandgap close to 1.6 eV [4]. The success of CIGS technology still depends on the availability of indium as a key element in the CIGS production line. This element has been considered for years as a scarce earth element, but the latest analysis indicates that indium resource availability could not impact the CIGS production [5].

As indium has been considered a scarce earth material for a long time, researchers in the field of thin-film solar cells started to explore a new earth abundant material. In this regard, recently, the kesterite (Cu_2ZnSnS_4 noted CZTS or $Cu_2ZnSnSe_4$ noted CZTSe) has generated considerable interest. This family of materials (copper, zinc, tin and sulfide or selenide) is thus becoming a promising new material for the development of eco-friendly solar cells. This innovative technology has rapidly improved in recent years; however, its performance still suffers from low conversion efficiency.

The best efficiencies of kesterite solar cells are 12.6% for $Cu_2ZnSn(S,Se)_4$, 12.5% for $Cu_2ZnSnSe_4$, 11% for Cu_2ZnSnS_4 and recently 13% for $(Ag_xCu_{1-x})_2ZnSn(S,Se)_4$ [6–9]. The efficiency of kesterite is limited by the large V_{oc} deficit (E_g/q– V_{oc}), which can be attributed to absorber-related defects, i.e. anti-site defect, cationic disorder, band tailing and optical and

* e-mail: charif.tamin@insa-lyon.fr

electrostatic fluctuations [10–13]. Indeed, kesterite absorbers, copper (Cu) and zinc (Zn) cations have a close ionic radius, which leads to a partial disorder in the Cu-Zn plane [14,15]. The result a Cu_{Zn} and Zn_{Cu} anti-site defect, which seems to be the main origin to electrostatic fluctuations [16]. In addition, there is a considerable deficit in the electronic interfaces in kesterite solar cells. It is known that band alignments interfaces are critical issues for solar cell performance, but in the kesterite community there are still few experimental studies conducted to investigate this issue.

According to the literature available, there is an unfavorable conduction band offset (CBO) at the buffer/absorber interface, resulting in a significant V_{oc} deficit in kesterite [17,18]. In general, CZTS sulfide solar cells form a type II heterojunction at the buffer/absorbers interface, resulting in a negative CBO (cliff-like) [19]. Typically, the ideal band alignment for heterojunction solar cells is type I, with a slightly positive CBO (spike-like) [10]. However, if the spike becomes too high, the photogenerated electrons flowing from the absorber to the upper contact will be blocked by a large electronic barrier at the heterojunction interface. Therefore, the fundamental issues related to absorber and heterojunction need more in-depth study to further develop the potential of these kesterite-based solar cells.

To this end, several research works have used a new approach based on the partial and/or complete substitution of Cu and/or Zn by cations of larger radius to minimize/suppress any problems associated with the Cu-Zn disorder. Some research has reported that partial substitution of Cu by Ag and Zn by Cd can improve several properties of the absorber and the device, namely improvement of grain size, minimization of anti-site defects and increase in conversion efficiency [20–24]. However, the use of Ag and Cd still directs research towards the use of toxic and/or expensive elements in solar cells, which deviates from the main goal of developing eco-friendly solar cells. The effects of partial cation substitution in CZTS have so far been extensively studied in terms of their effect on the bulk absorber and the efficiency of the solar cell, with less emphasis on their effect on the band alignment. In this regard, several researchers have reported the use of new wide-band gap buffers to address band alignment issues. Significant improvements in V_{oc} have been achieved by using $Zn_{1-x}Sn_xO$ and $Cd_{1-x}Zn_xS$ as buffer layers [25–27]. However, the V_{oc} deficit is still too large.

This work presents the cation substitution strategy where the partial substitution of Zn by Cd and Mn is highlighted. First, the effects of substitution on the morphology, crystalline structure, band gap and positions of the valence bands in these absorbers are presented. Then, the impact of cation substitution on band alignment is studied to adjust the interface properties and to form a favorable CBO only by partial substitution of Zn with Cd and Mn, which to our knowledge, has never been reported before. Finally, the last section concludes this work.

2 Materials and methods

2.1 Thin films preparation

2.1.1 Absorbers

Thin films of Cu_2ZnSnS_4 (pure), $Cu_2Zn_{1-x}Cd_xSnS_4$ (Cd substitution) and $Cu_2Zn_{1-x}Mn_xSnS_4$ (Mn substitution) absorbers were coated by a sol–gel spin coating with $x = 0.15$. These absorber samples are referred to as CZTS, CCZTS and CMZTS, respectively. A sol–gel solution of pure CZTS was made by dissolving copper acetate monohydrate, zinc acetate dihydrate, tin chloride dihydrate and thiourea (H_2NCSNH_2) in 2-methoxyethanol as solvent at concentrations of 0.46 M, 0.27 M, 0.25 M and 2 M, respectively. A few drops of di-ethanolamine were then added to the solution to stabilize it. The molar ratio of precursors was maintained as follows: $Cu/Sn = 1.84$, $Zn/Sn = 1.08$ and $S/metal = 2$. The solution was stirred for 6 h at 50 °C until a dark yellow solution was formed.

For the partial substitution of Zn by Cd and Mn, two new solutions were prepared following the protocol previously used for CZTS. Cadmium acetate dihydrate was used as the Cd source and manganese chloride tetrahydrate as the Mn source. The $Cd/(Cd+Zn)$ and $Mn/(Mn+Zn)$ ratios were taken at 0.15 each. Thin layers of CZTS, CCZTS and CMZTS were deposited on glass substrates from sol-gel solutions using spin coating at 4000 rpm for 30 s. The samples were then dried in a furnace heated to 250 °C for 3 min. This process was repeated 5 times to obtain a thick film. Finally, the samples were again heat treated in a sulfurization furnace at 520 °C for 30 min where the ramp rate was 10 °C/min. This final process was performed in the presence of sulfur powder (1.2 g) under nitrogen gas flow. The final thickness of the films after heat treatment was ∼500 nm.

2.1.2 Heterojunction

The heterojunctions were produced by chemical bath deposition (CBD) of CdS buffer layers on CZTS, CCZTS and CMZTS absorbers. The chemicals used in the bath reaction were cadmium acetate dihydrate, thiourea and ammonia with concentrations of 0.03 M, 0.15 M and 1.2 M respectively, all chemicals were mixed in deionized water. The CBD process took 10 min at 70 °C, and the pH of the solution was maintained around 10. After CdS deposition, the heterojunction samples were dried with only a nitrogen gas flow without any heat treatment. These heterojunction samples are respectively referred to as CZTS/CdS, CCZTS/CdS and CMZTS/CdS.

2.2 Characterization

A scanning electron microscope (SEM) was used to study the surface morphology of the films. The observations were performed by a Hitachi SU8230 SEM at an accelerating voltage of 15 keV. X-ray diffraction (XRD) was used to study the crystal structures of the films in $\theta/2\theta$ scanning mode. The analysis was performed with a Bruker D8 DISCOVER ($CuK\alpha_1$ radiation, $\lambda = 1.54056$ Å). A custom-built epi-confocal microscope equipped with a 40x objective (0.6, Nikon) was used for Raman analysis in order to confirm the purity of phases. The samples were exposed to a laser excitation wavelength of 784 nm. Raman spectra were acquired using a spectrometer (equipped with a 1200 lines/mm array) associated with a cooled CCD camera (1024×256 pixels). A wafer of silicon (111) was used for the calibration at 520 cm^{-1}. The absorption coefficient and band gap were derived from UV/Visible according to the

Tauc model. UV/Visible spectrophotometer (Thermo Spectronic Helios Gamma) was used to collect the transmission rate of each absorber sample as a function of wavelength. The analysis wavelength area ranged between 200 nm and 1100 nm with a step of 0.5 nm.

The valence band offset (VBO) measurements at the buffer/absorber heterojunctions were performed using an XPS PHI Versaprobe 5000 instrument equipped with the Al monochromator Kα_1 ($h_v = 1486.6$). The depth profile data was obtained by applying a mild argon sputtering (at 500 eV) to minimize the influence of ion bombardment on the buffer/absorber heterojunctions. The sputtered area was 2 mm × 2 mm and the analysis spot was 200 µm. The photoemission spectra of the valence band (VB) near fermi level (0 eV) data were collected every 60 s of etching time. The linear region of the near fermi level photoemission spectra was used for extrapolation to estimate the VB position. The spectra were processed using the Edge Down Background type in Casa XPS. The combination of the XPS analysis of the VBO and the UV/Visible measurement of the band gap allowed to estimate the band alignments at the absorber/buffer heterojunctions and to calculate the conduction band offset (CBO).

Time resolved photoluminescence (TRPL) was measured on heterojunction samples using the time correlated single photon counting technique [28]. This system is based on a custom-built epi-confocal microscope (Nikon, Eclipse Ti) scanned with a piezoelectric translation stage (Mad City Labs, Nano-LP100). The carriers generated at the heterojunction interface and at the upper part of the absorber region were excited by a 485 nm pulsed laser diode (PicoQuant, LDH-DC-485, with a pulse width < 90 ps and a repetition rate of 20 MHz) focused with a 40× air-objective (NA = 0.6, Nikon). An average intensity power of 0.6 µW was applied. The resulting photoluminescence was selected with a bandpass filter and detected with an APD (Excelitas, SPCM-AQRH-15) with a time resolution of 300 ps. The luminescence intensity decays were recorded with a dedicated electronic system (PicoQuant, PicoHarp300).

3 Results and discussion

This section discusses the effects of the partial substitution of zinc (Zn) by cadmium (Cd) and manganese (Mn) on morphological, structural, optical and electronic properties. Experimental band alignment and recombination at the heterojunctions produced with these absorbers (CZTS, CCZTS and CMZTS) and CdS buffer layer were investigated. The experimental optical and electronic results were modeled by SCAPS to get an overview of the effect of CBO on the photovoltaic conversion efficiency.

3.1 Morphological and structural characterization

An SEM analysis was performed to obtain information on the effect of substitution on the surface morphology of absorbers. Figure 1 shows the top view of the CZTS, CCZTS and CMZTS samples with two different magnifications, one lower and one higher. The low magnification images clearly

show the absence of cracks in the films for all samples. At a higher magnification, there is a noticeable decrease in voids due to Cd and Mn substitution and an improvement in surface grain size for the CCZTS and CMZTS samples. As the cross-section images are not included in this work, we cannot conclude if the grain size in the bulk absorbers shows a similar improvement as in the surface grain size or no. Figure 2a shows the XRD pattern of the CZTS, CMZTS and CCZTS samples. The common diffraction main peaks for the samples correspond to planes (112), (220) and (312) with a preferential direction along the plane (112). There are no secondary phases for the CZTS and CMZTS samples, whereas the CCZTS sample presents an additional secondary phase which corresponds to tin di-sulfide. The lattice parameters derived from the Rietveld X-ray analysis of CZTS, CCZTS, and CMZTS are shown in Figure 2b and Table 1. The lattice constants a and c are larger for CCZTS compared to CZTS, while those constants are smaller for CMZTS compared to CZTS and CCZTS. This behavior may be due to the larger radius of Cd^{2+} and smaller radius of Mn^{2+} compared to Zn^{2+}. Using XRD alone, it is difficult to distinguish between the coexisting phases in the kesterite system. Therefore, Raman spectroscopy was used to confirm the phase purity of the grown thin films. The Raman spectra for CZTS, CCZTS and CMTS under excitation by a laser of 784 nm are shown in Figure 3.

Figure 3a shows the Raman spectra of the CZTS sample. The appearance of the high-intensity peaks at about 288 cm^{-1} and 337.5 cm^{-1} corresponds to the two A modes of the kesterite structure whereas the less intense peaks at 366.3 cm^{-1} and 373 cm^{-1} correspond to the E(LO) and B(LO) modes [29–32]. Figure 3b shows the Raman spectra of the CCZTS sample. Two peaks are observed, one most intense at 334.4 cm^{-1} which corresponds to the A mode and the other at 365.6 cm^{-1} which correspond to E (LO) mode [33]. However, the second intense A mode does not appear near 287 cm^{-1}. The absence of this peak may be due to the cation rearrangement which leads to a new symmetry of the crystalline structure. Dimitrievska et al. reported that the presence of a peak near 334 cm^{-1} may be due to the presence of the kesterite phase with P42c symmetry [33]. This symmetry differs from that of kesterite I-4 in the cation arrangement. Figure 3c shows the Raman spectra of the CMZTS sample. As for the CZTS sample, this spectrum is characterized by the two modes A corresponding to the intense peaks at 289 cm^{-1} and 338.8 cm^{-1}. In addition, the CMZTS spectrum contains the E(LO) and B(LO) modes, which correspond to the less intense peaks at 367.7 cm^{-1} and 374.2 cm^{-1}, respectively [34]. No peaks corresponding to ZnS (at 348 cm^{-1}), Cu$_{2-x}$S (at 476 cm^{-1}), SnS$_2$ at (315 cm^{-1}) and Cu$_2$SnS$_3$ (at 352 cm^{-1}) are present in all samples [35–40]. The absence of peaks corresponding to the SnS2 phase in the Raman spectrum of CCZTS may be due to the employment of an unsuitable laser to detect this secondary phase.

3.2 Band gap and valence band energies

The absorption coefficient and band gap (BG) derived from the Tauc model were compared to examine whether partial
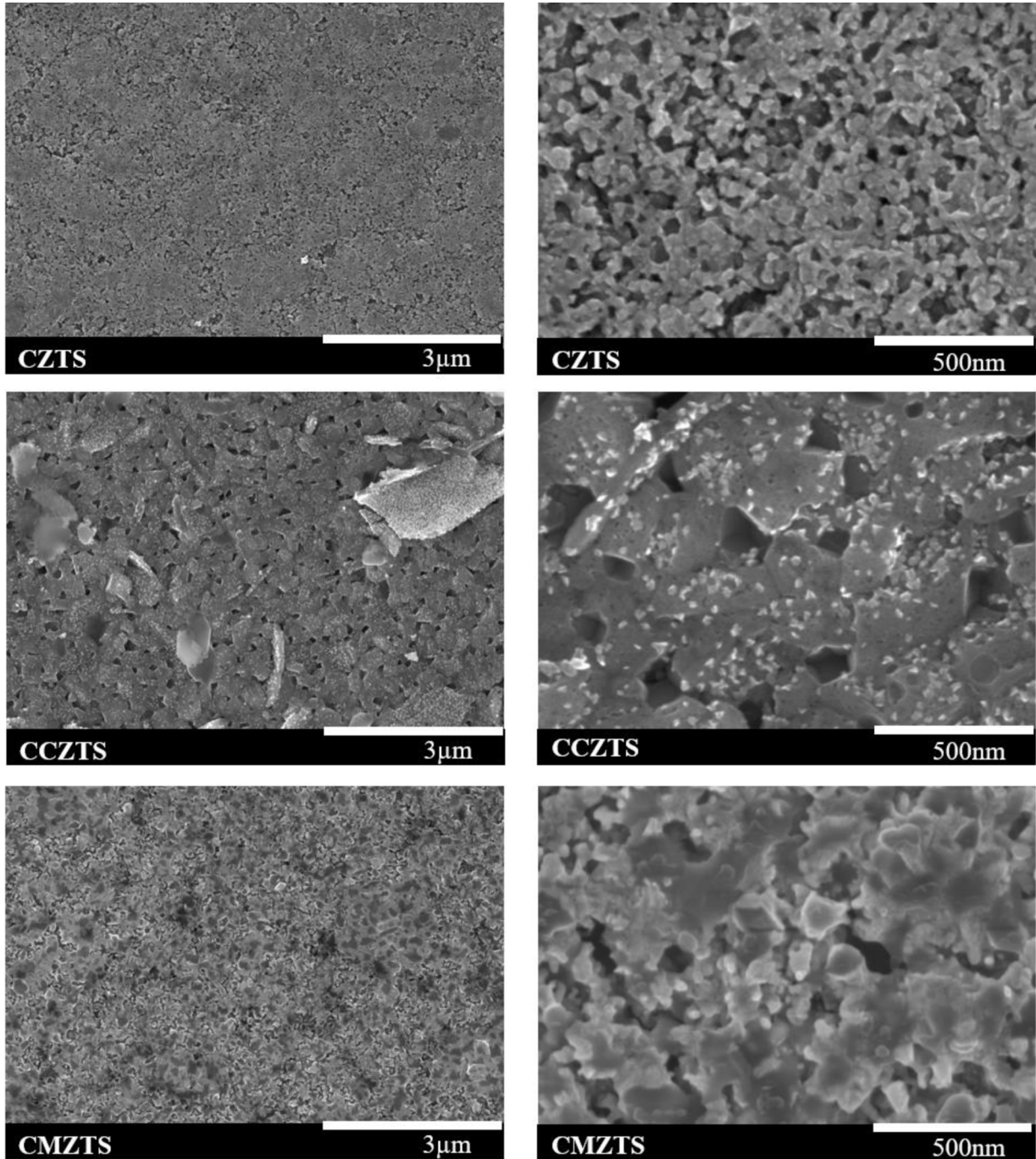
Fig. 1. SEM micrographs of CZTS, CCZTS and CMZTS samples.

cation substitution affects optical properties. The Tauc formula is given as follows:

$$(\alpha h\upsilon)^2 = A(h\upsilon - E_g), \qquad (1)$$

where α is the absorption coefficient, h is the Planck's constant, υ is the frequency, A is the constant and E_g is the band gap energy.

The absorption coefficient is given by:

$$\alpha = \frac{1}{e}\ln\left(\frac{1}{T}\right), \qquad (2)$$

where e is the layer thickness and T is the transmittance.

Figure 4 shows the band gap and absorption coefficients of CZTS, CCZTS and CMZTS obtained from UV/Visible measurements. In the pure CZTS sample,
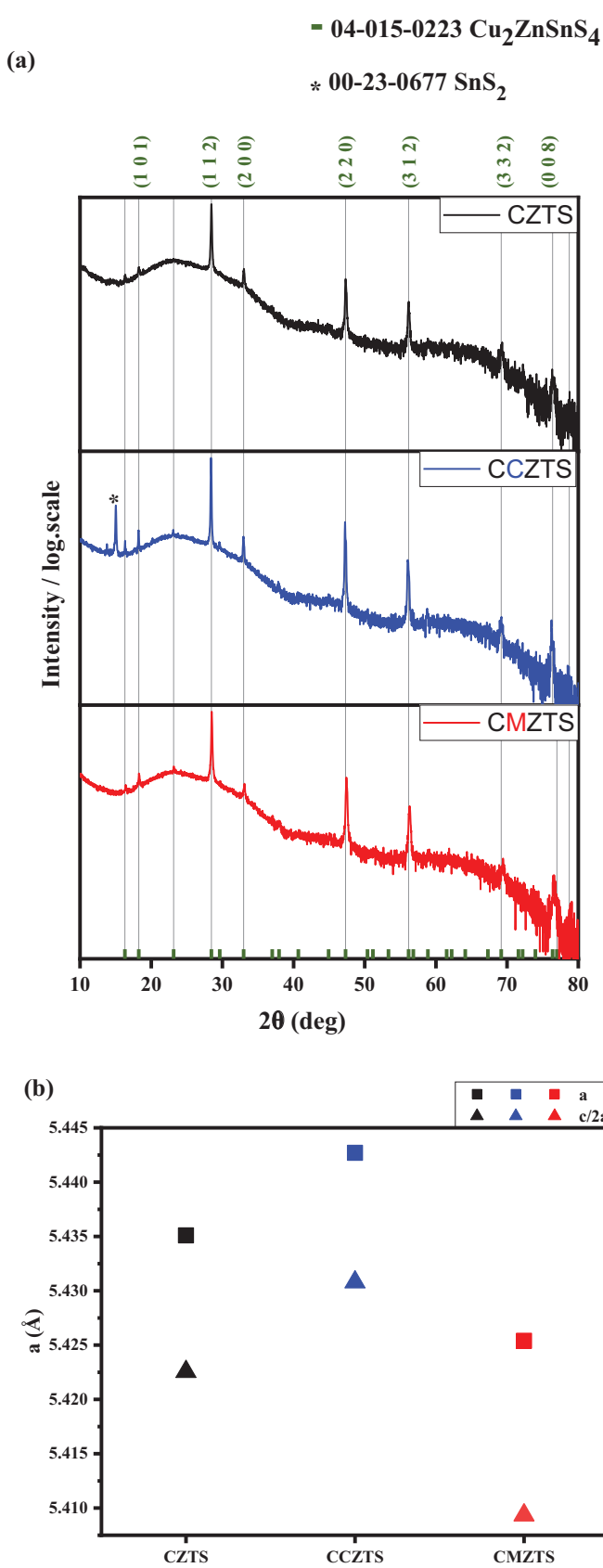
Fig. 2. X-ray diffractogram (a) and lattice parameters (b) of CZTS, CCZTS and CMZTS samples.

Table 1. Lattice parameters of CZTS, CCZTS and CMZTS samples obtained by Rietveld X-ray analysis.

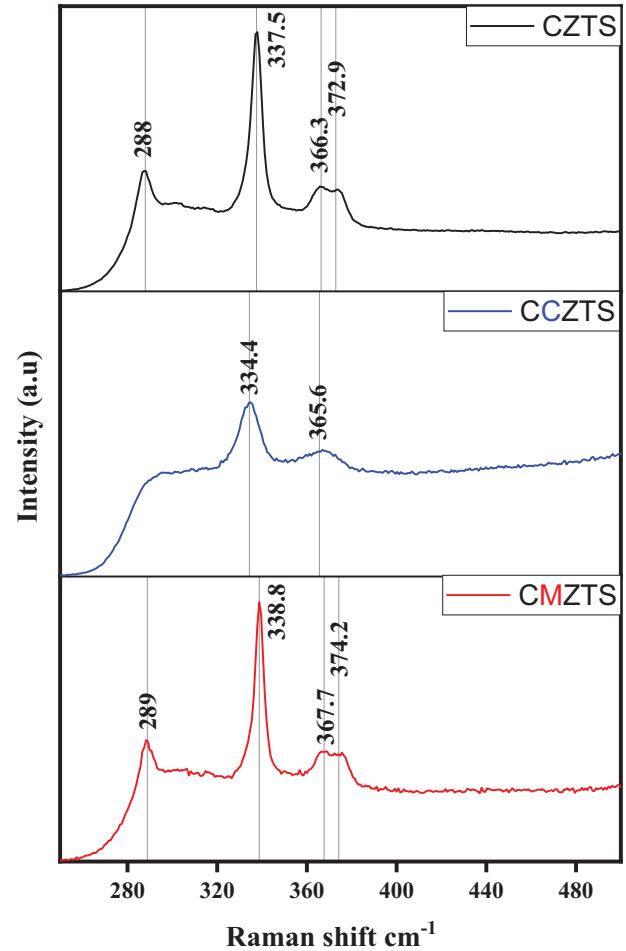| Samples	a (Å)	c (Å)
CZTS	5.4351	10.8451
CCZTS	5.4427	10.8616
CMZTS	5.4254	10.8187

Fig. 3. Raman spectra for CZTS, CCZTS and CMTS samples.

the energy in the band gap is about 1.55 eV while the absorption coefficient near the band gap is about 1×10^4 cm^{-1} and 3.8×10^4 cm^{-1} at 3 eV, which is the maximum absorption value. However, when Cd is alloyed in the CCZTS sample, the energy of the band gap decreases to about 1.43 eV compared to the CZTS sample, where the absorption coefficient at 1.43 eV remains about 1×10^4 cm^{-1}, and the maximum absorption at 3 eV becomes 4.6×10^4 cm^{-1}. In the CMZTS sample, when manganese is added, the energy of the band gap increases to about 1.62 eV compared to the CZTS sample, with an absorption coefficient at 1.62 eV of about 1×10^4 cm^{-1}, however at 3 eV the maximum absorption coefficient become 5.5×10^4 cm^{-1}, which is much higher than the pure CZTS and CCZTS samples.

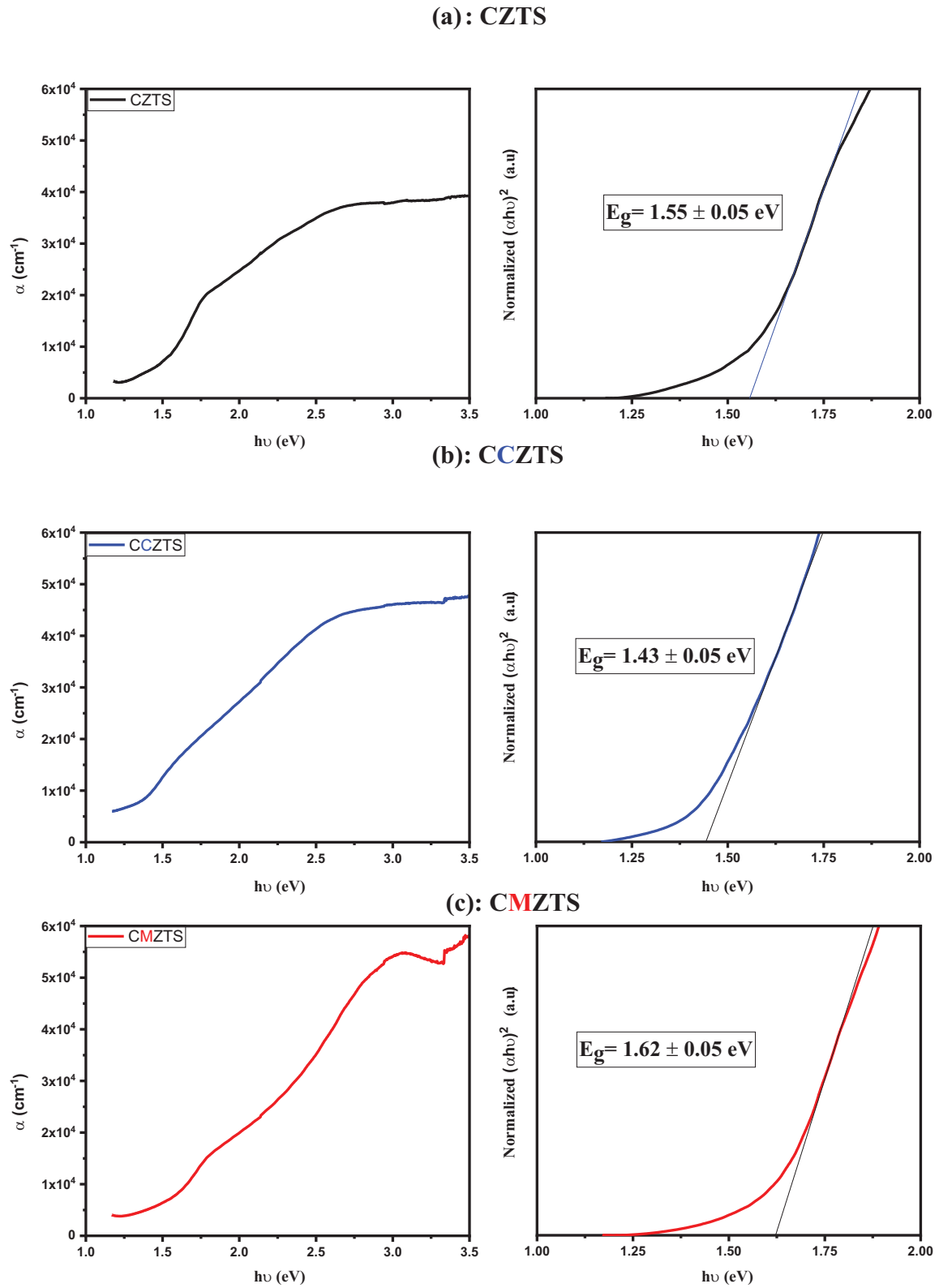**(a) : CZTS**

(b): CCZTS

(c): CMZTS

Fig. 4. Estimation of the band gap and the absorption coefficient from the UV/Visible measurement. (a) CZTS, (b) CCZTS, (c) CMZTS.

The partial substitution of Zn in the CZTS allows the band gap to be adjusted to a lower energy by Cd incorporation and to a higher energy by Mn incorporation. With respect to the absorption coefficient, the partial substitution of Zn increases the absorbance almost on the lower wavelength, for both Cd and Mn incorporation. This raises a potential interest to develop kesterite solar cells with a gradual band gap and change the unfavorable CBO type only by partial cation substitution. The optical band gap derived from the Tauc plot represents the energy difference between the valence band (VB) and the conduction band (CB).

According to the previous observation, the partial substitution of Zn adjusts the band gap to a lower energy by Cd incorporation and to a higher energy by Mn incorporation. However, it is not clear whether this adjustment is due to a shift of the CB position only, or due to a shift of the VB position as well. Therefore, the VB positions of CZTS, CCZTS and CMZTS were studied using the XPS measurement. Figure 5 shows the valence band spectra of the bulk films. From the VB spectra, the VB position of CZTS is about -0.17 eV; this position decreases in CCZTS to about -0.20 eV and to about -0.33 eV in CMZTS. It can be noted that the position at 0 eV in the VB spectra represents the fermi level energy (E_F); all values above E_F are negative.

Figure 6 shows the VB and CB positions of CCZTS and CMZTS in comparison with CZTS. It can be deduced from the figure that the partial substitution of Zn by Cd and Mn affects the VB position and/or the CB position. The VB position of CCZTS is 0.03 eV lower than the VB position of CZTS, but the band gap is 0.13 eV lower than that of CZTS. This means the partial substitution of Zn by Cd does not contribute too much on the VB position but contribute much more on the CB position to reduce the band gap. The VB position of CMZTS is 0.16 eV lower than the VB position of CZTS, but the band gap is 0.07eV higher than CZTS. Since Mn alloy reduces the VB position and does not increase it, and since the band gap increases by Mn incorporation, it is clear that the CMZTS band gap adjustments are mainly due to the modification of VB and CB positions with more contribution on the VB position which may be due to a lower doping level for CMZTS sample.

These results open the way for design of kestetie-based solar cells with gradual band gap as well as the modification of the unfavorable cliff like CBO only by partial cations substitution.

3.3 Heterojunctions band alignments

Since the partial substitution of Zn by Cd and Mn affects the VB and CB positions, it is interesting to know their effect on the band alignment at the absorber/buffer heterojunctions, and to estimate the valence band offset (VBO) and the conduction band offset (CBO) of the heterojunctions. An ideal band alignment for heterojunction solar cells is a slightly positive CBO (spike-like). In
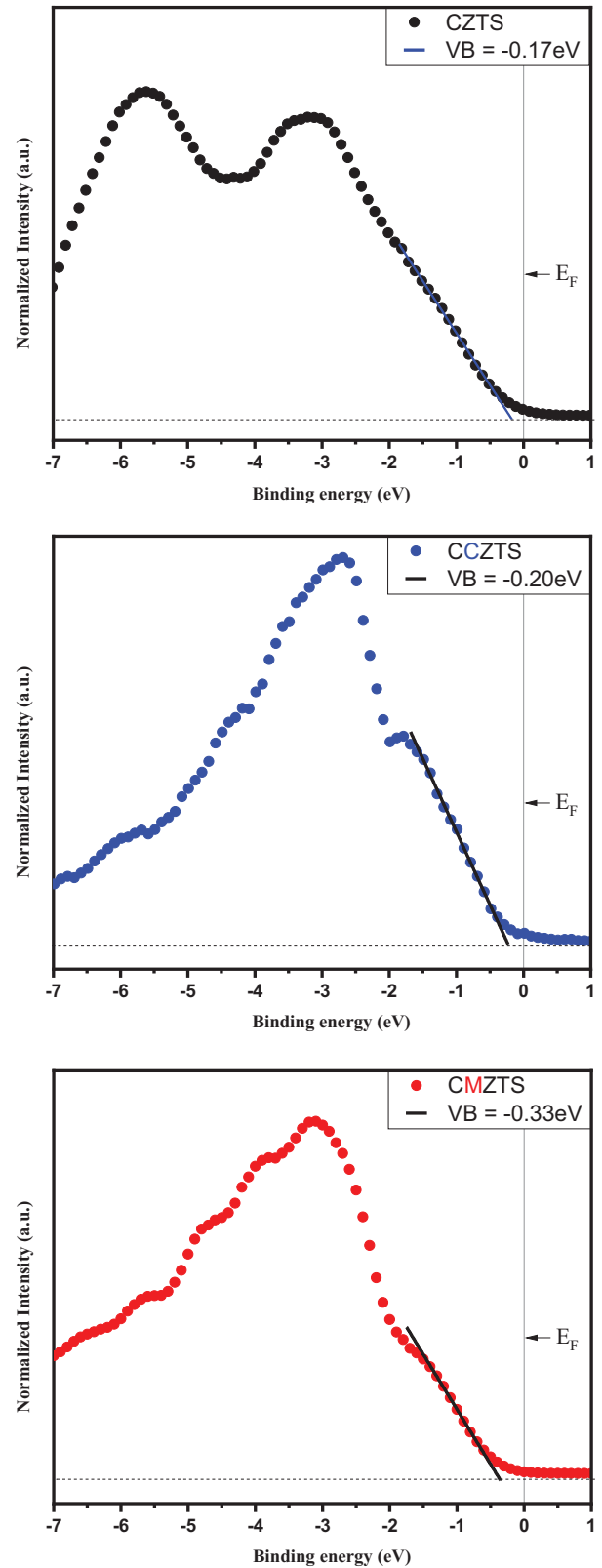

Fig. 5. Estimation of the valence band position from XPS measurement. (a) CZTS, (b) CCZTS, (c) CMZTS.
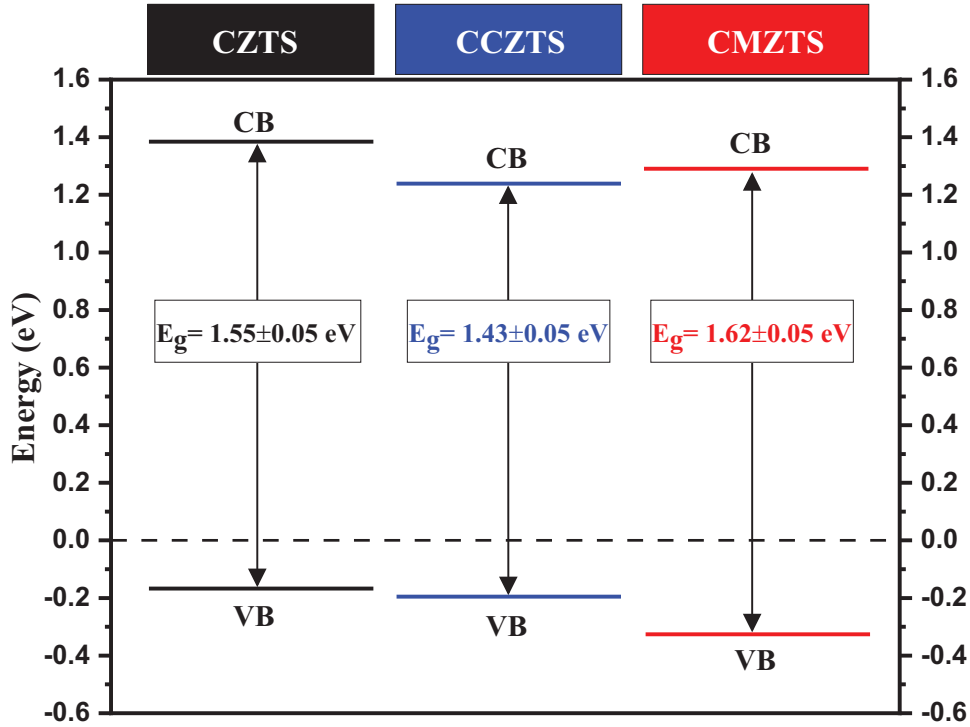
Fig. 6. Valence and conduction band positions of CZTS, CCZTS and CMZTS.

their theoretical work on CIGS chalcopyrite solar cells, Minemoto et al. (2001) argued that high efficiencies can be achieved only when the CBO at the CIGS/CdS hetero-junction varies between 0 and 0.4 eV [41]. In the case of pure sulfide CZTS, the CBO at the CZTS/CdS hetero-junction is rather negative (cliff-like), however, reported experimental values vary considerably. According to the literature, most reported experimental values of CBO at the CdS/CZTS heterojunction range between −0.34 eV and 0 eV, as shown in Figure 7a [8,32,42–48]. Haight et al. reported a positive (spike-like) CBO of +0.41 eV [49]. Recently, Su et al. (2020) reported an optimal near-flat band CBO of +0.05 eV using the strategy of Cd incorporation and device annealing [50]. In addition, the authors achieved the new world record (no certified) of 12.6% using this approach.

Figure 7b shows the variation of CBO as a function of device efficiency reported in the literature. An overall correlation can be established between the CBO measured at the absorber/buffer heterojunction by the different groups: low efficiency cells often have a large negative CBO, whereas most high efficiency cells have an almost flat band. It is important to note that only the pure sulfide kesterite alloys are described in this paper along with estimated VBO values obtained by direct XPS measure-ment of the VB positions across the interface buffer/absorber. In this sense, the CdS was used as a buffer layer to form heterojunctions with the absorbers (CZTS, CCZTS and CMZTS). The measurements were performed by XPS through the heterojunction from the upper layer (buffer) to the lower layer (absorber). Low-energy argon sputtering (500 eV) was used to etch

the heterojunction to reach the interface (for more information on the determination of the VB at the interface, please refer to our previous paper [51]). The VBO is distinguished by the difference between the VB position of the buffer and the VB position of the absorber at the interface, as follows:

$$VBO = VB_{b(i)} - VB_{a(i)}, \tag{3}$$

where $VB_{b(i)}$ is the buffer layer VB position and $VB_{a(i)}$ is the absorber layer VB position.

Figure 8 shows the valence band spectra at the interface of the CdS/CZTS, CdS/CCZTS and CdS/CMZTS heterojunctions. The value of the VBO at the CdS/CZTS heterojunction is about −1.01 eV, while this value becomes about −0.77 eV in the case of the CdS/CCZTS hetero-junction. This value then becomes about −0.72 eV at the CdS/CMZTS heterojunction. It is important to note that this estimation method does not consider the possible charge/dipole effects at the interface between the absorber and the buffer which may can modify the real VBO values.

Using equation (4), the CBO values were determined by combining the VBO values obtained from XPS and the band gap differences between the buffer and absorber layers that were measured from the Tauc plot by UV–visible spectrophotometer on all four samples (CdS, CZTS, CCZTS and CMZTS)

$$CBO = (E_g^b - E_g^a) + VBO \tag{4}$$

where E_g^b is the buffer layer band gap and E_g^a is the absorber layer band gap.
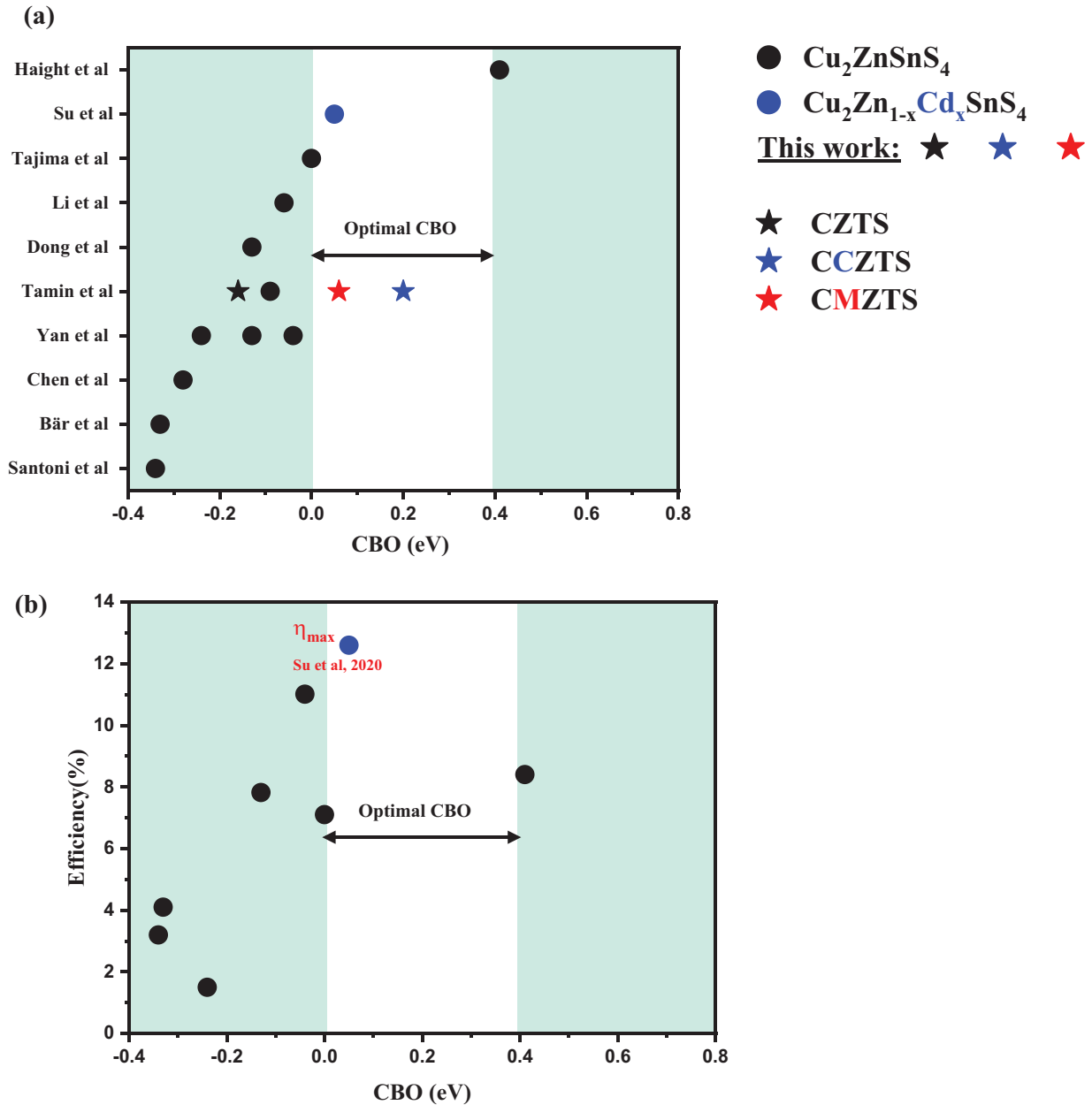
(a)

(b)

Fig. 7. (a) An overview of all the experimental work reported in the literature on the CBO value of pure sulfide keserite. (b) An overview of the performance of solar cells based on pure sulfide in the literature as a function of CBO value.

The CBO at the CdS/CZTS heterojunction was $-0.16\,\text{eV}$; this value was increased in the case of the CdS/CCTS heterojunction by Cd incorporation to $+0.20\,\text{eV}$, while in the case of CdS/CMZTS heterojunction with Mn incorporation, the CBO was increased to $+0.06\,\text{eV}$ in comparison to CdS/CZTS heterojunction. It is thus evident that the partial substitution of Zn by Cd and Mn has a significant influence on the CBO. Moreover, it is important to note that the CBO calculations were performed based on the band gap of pure materials without considering the interdiffusion effect at the interface, which can modify the band gaps.

Figure 9 shows the band alignment diagram of the heterojunctions, based on the previously discussed results of VB, VBO, CBO and band gap. A negative CBO (cliff-like), which corresponds to a type II heterojunction, can be observed for the CdS/CZTS heterojunction. This result is in good agreement with previous studies that have reported a cliff-like CBO in the CdS/CZTS heterojunction. However, in the case of the CdS/CCZTS heterojunction, the CBO becomes positive (spike-like), which corresponds to a type I heterojunction. A similar observation concerns the CdS/CMZTS heterojunction, which presents a small spike-like CBO, giving an almost flat type heterojunction.
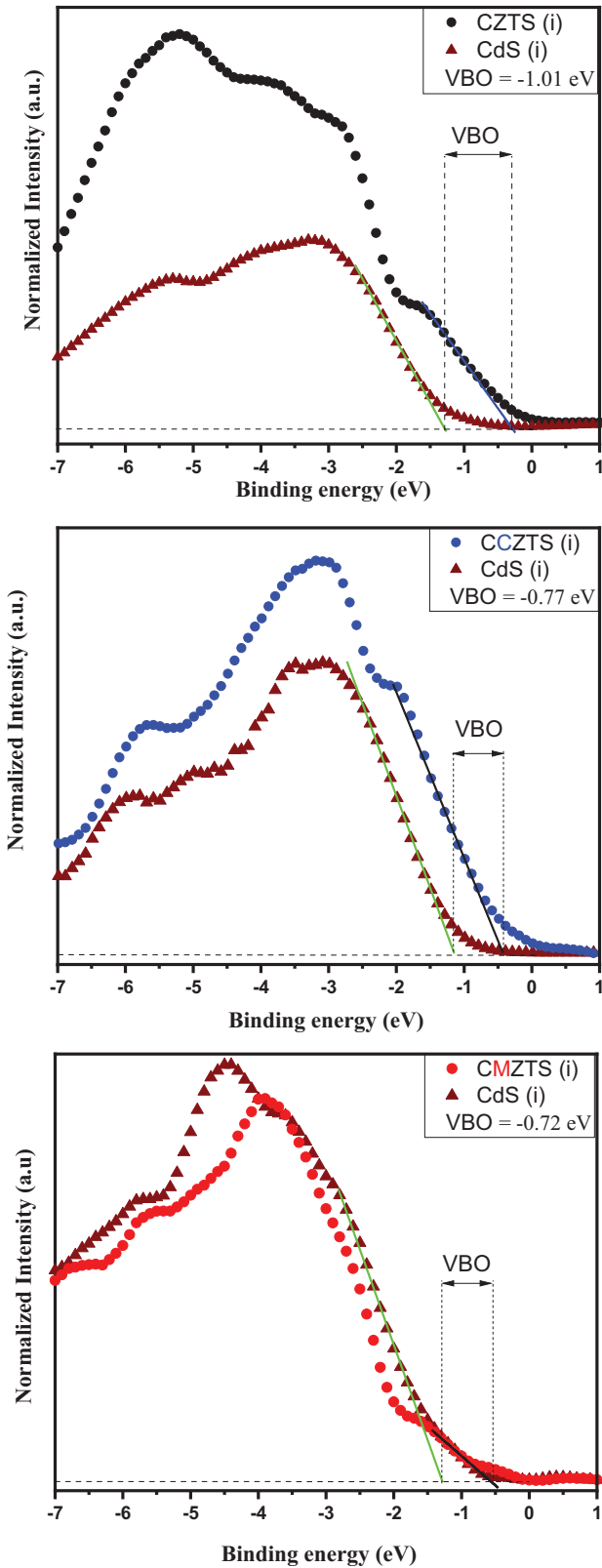
Fig. 8. Estimation of VBO at the absorber/buffer hetero-interface by direct XPS measurement. (a) CZTS/CdS, (b) CCZTS/CdS, (c) CMZTS/CdS.
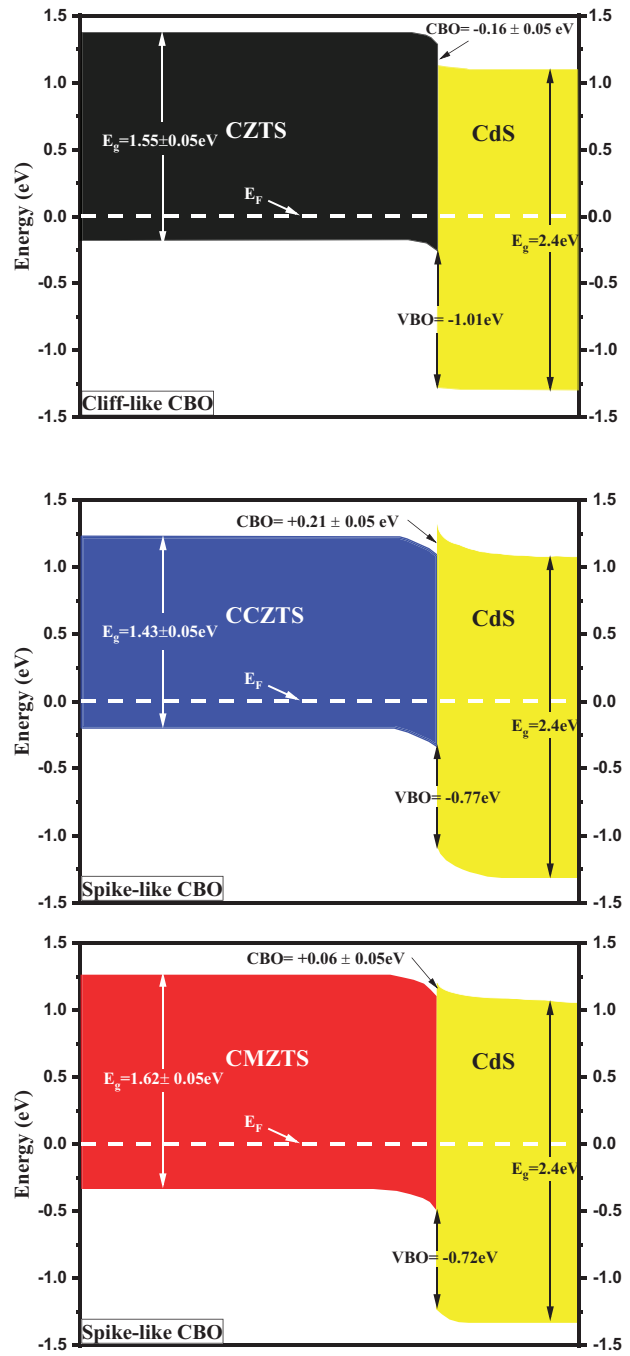

Fig. 9. Experimental band alignment at absorber/buffer hetero-junction. (a) CZTS/CdS, (b) CCZTS/CdS, (c) CMZTS/CdS.

Therefore, alloying CZTS by Mn and Cd improves band alignment in the case where the heterojunction occurs with CdS as a buffer layer, resulting in favorable band alignment within an optimal CBO range.

3.4 Time-resolved photoluminescence

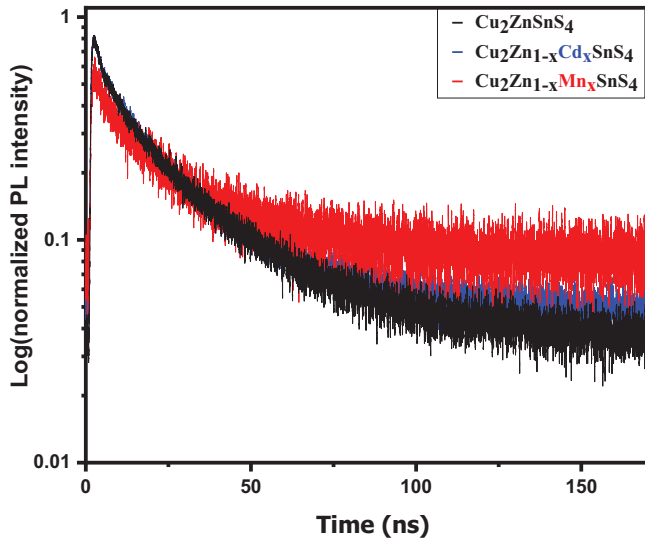Due to the significant improvement in band alignment with the partial substitution of zinc by Cd and Mn, it is

Fig. 10. Normalized and time-resolved photoluminescence decay with excitation wavelengths of 488 nm. Black color CZTS/CdS, blue color CCZTS/CdS and red color CMZTS/CdS.

interesting to study the recombination mechanism at the heterojunctions. To this end, TRPL measurements were used to characterize the recombination at the heterojunction. Yan et al. (2018) found a longer heterojunction lifetime due to the thermal treatment of the heterojunctions to promote cadmium diffusion into the upper region of the absorber [8]. The authors achieved the highest efficiency (certified world record) of pure sulfide CZTS solar cells using this approach. The same TRPL heterojunction characterization approach has been used in the present work. A 488 nm laser excitation was used to generate carriers at the heterojunction interface and in the upper absorber region. Figure 10 shows the TRPL spectra of the CZTS, CCTS and CMZTS samples. The decay time was adjusted using the bi-exponential function [52], as follows:

$$I(t) = A_1 \exp(-t/\tau_1) + A_2 \exp(-t/\tau_2). \quad (5)$$

The lifetime was derived from the bi-exponential function, as follows:

$$\tau = \frac{A_1 \tau_1 + A_2 \tau_2}{A_1 + A_2}, \quad (6)$$

where τ_1 represents the fast decay time, τ_2 represents the slow decay time, while A_1 and A_2 represent the amplitudes of τ_1 and τ_2, respectively, and τ represents the derived lifetime.

The TRPL spectra show almost similar PL decay times for CZTS and CCZTS samples, while the PL decay time increased by Mn incorporation in the case of CMZTS. Using equations (5) and (6), a lifetime of about 13 ns for CZTS and CCZTS and about 15 ns for CMZTS is obtained. Furthermore, it can be noted that the Mn alloying may reduce the recombination at the CMZTS/CdS heterointerface and improve charge separation, as reported by Lie et al. [53].

4 Conclusion

This paper investigated a cation substitution strategy in which the partial substitution of Zn by Cd and Mn was considered. A sol–gel process was used to perform a partial substitution of Zn in CZTS by Cd and Mn. It was demonstrated that alloying cadmium in CZTS improves grain size, reduces the band gap and adjusts the band alignment by forming an optimal spike-like CBO. However, the Mn alloy retains the pure kesterite phase, adjusts the band alignment to form a nearly flat CBO, which can facilitate charge separation at the p-n junction. Through this comparison, this study highlights an important strategy to improve the band alignment only by partial cation substitution. More detailed studies of the absorber/buffer heterointerface is required to establish the real band alignment by coupling photoemission spectroscopy (PES), inverse photoemission spectroscopy (IPES) and Kelvin probe force microscopy (KPFM).

Author contribution statement

C. Tamin conducted the experiments, the data analysis and wrote the manuscript. C. Tamin and D. Chaumont developed the idea, designed the experimental baseline and discussed the results. O. Heintz conducted the XPS measurements. A. Leray conducted the Raman and TRPL measurements. D. Chaumont and M. Adnane supervised the project. All authors reviewed and commented the manuscript according to their area of expertise.

References

1. K. Yoshikawa, H. Kawasaki, W. Yoshida, T. Irie, K. Konishi, K. Nakano, T. Uto, D. Adachi, M. Kanematsu, H. Uzu, K. Yamamoto, Silicon heterojunction solar cell with interdigitated back contacts for a photoconversion efficiency over 26%, Nat. Energy **2**, 17032 (2017)
2. M. Green, E. Dunlop, J. Hohl-Ebinger, M. Yoshita, N. Kopidakis, X. Hao, Solar cell efficiency tables (version 57), Prog. Photovolt. Res. Appl. **29**, 3 (2021)
3. M. Nakamura, K. Yamaguchi, Y. Kimoto, Y. Yasaki, T. Kato, H. Sugimoto, Cd-free Cu(In,Ga)(Se,S)2 thin-film solar cell with record efficiency of 23.35%, IEEE J. Photovolt. **9**, 1863 (2019)
4. N. Barreau, E. Bertin, A. Crossay, O. Durand, L. Arzel, S. Harel, T. Lepetit, L. Assmann, E. Gautron, D. Lincot, Investigation of co-evaporated polycrystalline Cu(In,Ga)S$_2$ thin film yielding 16.0% efficiency solar cell, EPJ Photovolt. **13**, 17 (2022)
5. E. Bellini, Indium supply not an issue for CIGS industry (n.d.). https://www.pv-magazine.com/2021/08/11/indium-supply-not-an-issue-for-cigs-industry/
6. W. Wang, M.T. Winkler, O. Gunawan, T. Gokmen, T.K. Todorov, Y. Zhu, D.B. Mitzi, Device characteristics of CZTSSe thin-film solar cells with 12.6% efficiency, Adv. Energy Mater. **4**, 1301465 (2014)

7. J. Li, Y. Huang, J. Huang, G. Liang, Y. Zhang, G. Rey, F. Guo, Z. Su, H. Zhu, L. Cai, K. Sun, Y. Sun, F. Liu, S. Chen, X. Hao, Y. Mai, M.A. Green, Defect control for 12.5% efficiency $Cu_2ZnSnSe_4$ kesterite thin-film solar cells by engineering of local chemical environment, Adv. Mater. **32**, 2005268 (2020)

8. C. Yan, J. Huang, K. Sun, S. Johnston, Y. Zhang, H. Sun, A. Pu, M. He, F. Liu, K. Eder, L. Yang, J.M. Cairney, N.J. Ekins-Daukes, Z. Hameiri, J.A. Stride, S. Chen, M.A. Green, X. Hao, Cu_2ZnSnS_4 solar cells with over 10% power conversion efficiency enabled by heterojunction heat treatment, Nat. Energy **3**, 764 (2018)

9. M.A. Green, E.D. Dunlop, J. Hohl-Ebinger, M. Yoshita, N. Kopidakis, X. Hao, Solar cell efficiency tables (version 59), Progr. Photovolt. Res. Appl. **30**, 3 (2022)

10. J. Li, D. Wang, X. Li, Y. Zeng, Y. Zhang, Cation substitution in earth-abundant kesterite photovoltaic materials, Adv. Sci. **5**, 1700744 (2018)

11. P. Bais, M.T. Caldes, M. Paris, C. Guillot-Deudon, P. Fertey, B. Domengès, A. Lafond, Cationic and anionic disorder in CZTSSe kesterite compounds: a chemical crystallography study, Inorg. Chem. **56**, 11779 (2017)

12. J. Bleuse, F. Ducroquet, H. Mariette, Potential fluctuations and localization effects in CZTS single crystals, as revealed by optical spectroscopy, J. Electr. Mater. **47**, 4282 (2018)

13. L. Grenet, M.A.A. Suzon, F. Emieux, F. Roux, Analysis of failure modes in kesterite solar cells, ACS Appl. Energy Mater. **1**, 2103 (2018)

14. Z.-K. Yuan, S. Chen, H. Xiang, X.-G. Gong, A. Walsh, J.-S. Park, I. Repins, S.-H. Wei, Engineering solar cell absorbers by exploring the band alignment and defect disparity: the case of Cu- and Ag-based kesterite compounds, Adv. Funct. Mater. **25**, 6733 (2015)

15. S. Schorr, The crystal structure of kesterite type compounds: a neutron and X-ray diffraction study, Solar Energy Mater. Solar Cells **95**, 1482 (2011)

16. T. Gokmen, O. Gunawan, T.K. Todorov, D.B. Mitzi, Band tailing and efficiency limitation in kesterite solar cells, Appl. Phys. Lett. **103**, 103506 (2013)

17. A. Crovetto, O. Hansen, What is the band alignment of $Cu_2ZnSn(S,Se)_4$ solar cells? Solar Energy Mater. Solar Cells **169**, 177 (2017)

18. S. Gao, Z. Jiang, L. Wu, J. Ao, Y. Zeng, Y. Sun, Y. Zhang, Interfaces of high-efficiency kesterite $Cu_2ZnSnS(e)_4$ thin film solar cells, Chin. Phys. B **27**, 018803 (2018)

19. X. Liu, Y. Feng, H. Cui, F. Liu, X. Hao, G. Conibeer, D.B. Mitzi, M. Green, The current status and future prospects of kesterite solar cells: a brief review: Kesterite solar cells, Prog. Photovolt: Res. Appl. **24**, 879 (2016)

20. M.H. Sayed, J. Schoneberg, J. Parisi, L. Gütay, Influence of silver incorporation on CZTSSe solar cells grown by spray pyrolysis, Mater. Sci. Semiconduct. Process. **76**, 31 (2018)

21. C. Yan, J. Huang, K. Sun, Y. Zhang, M.A. Green, X. Hao, Efficiency improvement of high band gap Cu_2ZnSnS_4 solar cell achieved by silver incorporation, in *2018 IEEE 7th World Conference on Photovoltaic Energy Conversion (WCPEC) (A Joint Conference of 45th IEEE PVSC, 28th PVSEC & 34th EU PVSEC)*, IEEE, Waikoloa Village, HI (2018), pp. 3709–3711

22. C. Yan, K. Sun, J. Huang, S. Johnston, F. Liu, B.P. Veettil, K. Sun, A. Pu, F. Zhou, J.A. Stride, M.A. Green, X. Hao, Beyond 11% efficient sulfide kesterite $Cu_2Zn_xCd_{1-x}SnS_4$ solar cell: effects of cadmium alloying, ACS Energy Lett. **2**, 930 (2017)

23. G. Gurieva, A. Franz, J.M. Prieto, T. Unold, S. Schorr, Structural and optoelectronic characterization of $(Ag_xCu_{1-x})ZnSnSe_4$ solid solution, in *2018 IEEE 7th World Conference on Photovoltaic Energy Conversion (WCPEC) (A Joint Conference of 45th IEEE PVSC, 28th PVSEC & 34th EU PVSEC)*, IEEE, Waikoloa Village, HI (2018), pp. 0808–0811

24. M.S. Kumar, S.P. Madhusudanan, S.K. Batabyal, Substitution of Zn in earth-abundant $Cu_2ZnSn(S,Se)_4$ based thin film solar cells − a status review, Sol. Energy Mater. Solar Cells **185**, 287 (2018)

25. X. Cui, K. Sun, J. Huang, C.-Y. Lee, C. Yan, H. Sun, Y. Zhang, F. Liu, Md.A. Hossain, Y. Zakaria, L.H. Wong, M. Green, B. Hoex, X. Hao, Enhanced heterojunction interface quality to achieve 9.3% efficient Cd-free Cu_2ZnSnS_4 solar cells using atomic layer deposition ZnSnO buffer layer, Chem. Mater. **30**, 7860 (2018)

26. J.K. Larsen, F. Larsson, T. Törndahl, N. Saini, L. Riekehr, Y. Ren, A. Biswal, D. Hauschild, L. Weinhardt, C. Heske, C. Platzer-Björkman, Cadmium free Cu_2ZnSnS_4 solar cells with 9.7% efficiency, Adv. Energy Mater. **9**, 1900439 (2019)

27. K. Sun, C. Yan, F. Liu, J. Huang, F. Zhou, J.A. Stride, M. Green, X. Hao, Over 9% efficient kesterite Cu_2ZnSnS_4 solar cell fabricated by using $Zn_{1-x}Cd_xS$ buffer layer, Adv. Energy Mater. **6**, 1600046 (2016)

28. C. Albrecht, Joseph R. Lakowicz, Principles of fluorescence spectroscopy, Anal. Bioanal. Chem. **390**, 1223 (2008)

29. B.G. Mendis, A.A. Taylor, M. Guennou, D.M. Berg, M. Arasimowicz, S. Ahmed, H. Deligianni, P.J. Dale, Nanometre-scale optical property fluctuations in Cu_2ZnSnS_4 revealed by low temperature cathodoluminescence, Solar Energy Mater. Solar Cells **174**, 65 (2018)

30. M. Dimitrievska, A. Fairbrother, X. Fontané, T. Jawhari, V. Izquierdo-Roca, E. Saucedo, A. Pérez-Rodríguez, Multiwavelength excitation Raman scattering study of polycrystalline kesterite Cu_2ZnSnS_4 thin films, Appl. Phys. Lett. **104**, 021901 (2014)

31. M. Paris, L. Choubrac, A. Lafond, C. Guillot-Deudon, S. Jobic, Solid-state NMR and Raman spectroscopy to address the local structure of defects and the tricky issue of the Cu/Zn disorder in Cu-poor, Zn-rich CZTS materials, Inorg. Chem. **53**, 8646 (2014)

32. C. Tamin, D. Chaumont, O. Heintz, R. Chassagnon, A. Leray, N. Geoffroy, M. Guerineau, M. Adnane, Investigation of absorber and heterojunction in the pure sulphide kesterite, Bol. Soc. Esp.Cerám. Vidr. **60**, 380 (2021)

33. M. Dimitrievska, F. Boero, A.P. Litvinchuk, S. Delsante, G. Borzone, A. Perez-Rodriguez, V. Izquierdo-Roca, Structural Polymorphism in "Kesterite" Cu_2ZnSnS_4: Raman spectroscopy and first-principles calculations analysis, Inorg. Chem. **56**, 3467 (2017)

34. G. Tseberlidis, V. Trifiletti, A. Le Donne, L. Frioni, M. Acciarri, S. Binetti, Kesterite solar-cells by drop-casting of inorganic sol-gel inks, Solar Energy **208**, 532 (2020)

35. A. Fairbrother, V. Izquierdo-Roca, X. Fontané, M. Ibáñez, A. Cabot, E. Saucedo, A. Pérez-Rodríguez, ZnS grain size effects on near-resonant Raman scattering: optical non-destructive grain size estimation, CrystEngComm. **16**, 4120 (2014)

36. R. Martí Valls, T. Stoyanova Lyubenova, I. Calvet Roures, L. Oliveira, D. Fraga Chiva, J.B. Carda Castelló, Easy and low-cost aqueous precipitation method to obtain $Cu_2ZnSn(S,Se)_4$ thin layers, Solar Energy Mater. Solar Cells **161**, 432 (2017)

37. P.A. Fernandes, P.M.P. Salomé, A.F. da Cunha, Growth and Raman scattering characterization of Cu_2ZnSnS_4 thin films, Thin Solid Films **517**, 2519 (2009)

38. R.B.V. Chalapathy, G.S. Jung, B.T. Ahn, Fabrication of Cu_2ZnSnS_4 films by sulfurization of Cu/ZnSn/Cu precursor layers in sulfur atmosphere for solar cells, Solar Energy Mater. Solar Cells **95**, 3216 (2011)

39. M.I. Khalil, R. Bernasconi, S. Ieffa, A. Lucotti, A. Le Donne, S. Binetti, L. Magagnin, Effect of co-electrodeposited Cu-Zn-Sn precursor compositions on sulfurized CZTS thin films for solar cell, ECS Trans. **64**, 33 (2015)

40. N.R. Mathews, J. Tamy Benítez, F. Paraguay-Delgado, M. Pal, L. Huerta, Formation of Cu_2SnS_3 thin film by the heat treatment of electrodeposited SnS-Cu layers, J Mater Sci: Mater Electron. **24**, 4060 (2013)

41. T. Minemoto, T. Matsui, H. Takakura, Y. Hamakawa, T. Negami, Y. Hashimoto, T. Uenoyama, M. Kitagawa, Theoretical analysis of the effect of conduction band offset of window/CIS layers on performance of CIS solar cells using device simulation, Solar Energy Mater. **67**, 83 (2001)

42. A. Santoni, F. Biccari, C. Malerba, M. Valentini, R. Chierchia, A. Mittiga, Valence band offset at the CdS/Cu_2ZnSnS_4 interface probed by X-ray photoelectron spectroscopy, J. Phys. D: Appl. Phys. **46**, 175101 (2013)

43. M. Bär, B.-A. Schubert, B. Marsen, R.G. Wilks, S. Pookpanratana, M. Blum, S. Krause, T. Unold, W. Yang, L. Weinhardt, C. Heske, H.-W. Schock, Cliff-like conduction band offset and KCN-induced recombination barrier enhancement at the CdS/Cu_2ZnSnS_4 thin-film solar cell heterojunction, Appl. Phys. Lett. **99**, 222105 (2011)

44. H.-J. Chen, S.-W. Fu, S.-H. Wu, T.-C. Tsai, H.-T. Wu, C.-F. Shih, Structural and photoelectron spectroscopic studies of band alignment at the Cu_2ZnSnS_4/CdS heterojunction with slight Ni doping in Cu_2ZnSnS_4, J. Phys. D: Appl. Phys. **49**, 335102 (2016)

45. Z.-Y. Dong, Y.-F. Li, B. Yao, Z.-H. Ding, G. Yang, R. Deng, X. Fang, Z.-P. Wei, L. Liu, An experimental and first-principles study on band alignments at interfaces of Cu_2ZnSnS_4/CdS/ZnO heterojunctions, J. Phys. D: Appl. Phys. **47**, 075304 (2014)

46. S. Tajima, K. Kataoka, N. Takahashi, Y. Kimoto, T. Fukano, M. Hasegawa, H. Hazama, Direct measurement of band offset at the interface between CdS and Cu_2ZnSnS_4 using hard X-ray photoelectron spectroscopy, Appl. Phys. Lett. **103**, 243906 (2013)

47. J. Li, Q. Du, W. Liu, G. Jiang, X. Feng, W. Zhang, J. Zhu, C. Zhu, The band offset at CdS/Cu_2ZnSnS_4 heterojunction interface, Electr. Mater. Lett. **8**, 365 (2012)

48. C. Yan, F. Liu, N. Song, B.K. Ng, J.A. Stride, A. Tadich, X. Hao, Band alignments of different buffer layers (CdS, Zn(O,S), and In_2S_3) on Cu_2ZnSnS_4, Appl. Phys. Lett. **104**, 173901 (2014)

49. R. Haight, A. Barkhouse, O. Gunawan, B. Shin, M. Copel, M. Hopstaken, D.B. Mitzi, Band alignment at the $Cu_2ZnSn(S_xSe_{1-x})_4$/CdS interface, Appl. Phys. Lett. **98**, 253502 (2011)

50. Z. Su, G. Liang, P. Fan, J. Luo, Z. Zheng, Z. Xie, W. Wang, S. Chen, J. Hu, Y. Wei, C. Yan, J. Huang, X. Hao, F. Liu, Device postannealing enabling over 12% efficient solution-processed Cu_2ZnSnS_4 solar cells with Cd^{2+} substitution, Adv. Mater. **32**, 2000121 (2020)

51. C. Tamin, D. Chaumont, O. Heintz, M. Adnane, Estimation of band alignment at CdS/CZTS hetero-interface by direct XPS measurements, Surf. Interface Anal. (2020). https://doi.org/10.1002/sia.6881

52. X. Wen, P. Yu, Y.-R. Toh, Y.-C. Lee, K.-Y. Huang, S. Huang, S. Shrestha, G. Conibeer, J. Tang, Ultrafast electron transfer in the nanocomposite of the graphene oxide-Au nanocluster with graphene oxide as a donor, J. Mater. Chem. C. **2**, 3826 (2014)

53. S. Lie, M.I. Sandi, Y.F. Tay, W. Li, J.M.R. Tan, D.M. Bishop, O. Gunawan, L.H. Wong, Improving the charge separation and collection at the buffer/absorber interface by double-layered Mn-substituted CZTS, Solar Energy Mater. Solar Cells **185**, 351 (2018)